

Kent Academic Repository

Full text document (pdf)

Citation for published version

Bryce, NS and Failes, TW and Stehn, JR and Baker, Karen and Zahler, S and Arzhaeva, Y and Bischof, L and Lyons, C and Dedova, I and Arndt, GM and Gaus, K and Goult, Benjamin T and Hardeman, Edna C. and Gunning, Peter W. and Lock, JG (2019) High content imaging of unbiased chemical perturbations reveals that the phenotypic plasticity of the actin cytoskeleton is constrained.

DOI

<https://doi.org/10.1016/j.cels.2019.09.002>

Link to record in KAR

<https://kar.kent.ac.uk/77329/>

Document Version

Author's Accepted Manuscript

Copyright & reuse

Content in the Kent Academic Repository is made available for research purposes. Unless otherwise stated all content is protected by copyright and in the absence of an open licence (eg Creative Commons), permissions for further reuse of content should be sought from the publisher, author or other copyright holder.

Versions of research

The version in the Kent Academic Repository may differ from the final published version.

Users are advised to check <http://kar.kent.ac.uk> for the status of the paper. **Users should always cite the published version of record.**

Enquiries

For any further enquiries regarding the licence status of this document, please contact:

researchsupport@kent.ac.uk

If you believe this document infringes copyright then please contact the KAR admin team with the take-down information provided at <http://kar.kent.ac.uk/contact.html>

1 High content imaging of unbiased chemical perturbations reveals
2 that the phenotypic plasticity of the actin cytoskeleton is
3 constrained

4 Nicole S. Bryce¹, Tim W. Failes², Justine R. Stehn¹, Karen Baker³, Stefan Zahler⁴, Yulia Arzhaeva⁵, Leanne
5 Bischof⁵, Ciaran Lyons¹, Irina Dedova¹, Greg M. Arndt², Katharina Gaus^{1,6,7}, Benjamin T. Goult³, Edna C.
6 Hardeman¹, Peter W. Gunning^{1@} and John G. Lock^{1#@}.

7 1. School of Medical Sciences, UNSW Sydney, NSW 2052, Australia

8 2. ACRF Drug Discovery Centre, Children's Cancer Institute, Lowy Cancer Research Centre, UNSW
9 Sydney, NSW 2052, Australia

10 3. School of Biosciences, University of Kent, Canterbury, Kent, CT2 7NJ, UK

11 4. Department of Pharmacy, Ludwig-Maximilians-University, Munich, Germany

12 5. Quantitative Imaging Research Team, CSIRO Data 61, Marsfield, NSW, Australia

13 6. EMBL Australia Node in Single Molecule Science, UNSW Sydney, NSW 2052, Australia

14 7. ARC Centre of Excellence in Advanced Molecular Imaging, UNSW Sydney, NSW 2052, Australia

15

16

17 # Lead contact

18 john.lock@unsw.edu.au

19 @ Denotes equal contribution

20

21 **Summary**

22 Although F-actin has a large number of binding partners and regulators, the number of phenotypic
23 states available to the actin cytoskeleton is unknown. Here, we quantified 74 features defining F-actin
24 and cellular morphology in >25 million cells after treatment with a library of 114,400 structurally
25 diverse compounds. After reducing the dimensionality of these data, only ~25 recurrent F-actin
26 phenotypes emerged, each defined by distinct quantitative features that could be machine learned.
27 We identified 2003 unknown compounds as inducers of actin-related phenotypes, including two that
28 directly bind the focal adhesion protein talin. Moreover, we observed that compounds with distinct
29 molecular mechanisms could induce equivalent phenotypes and that initially divergent cellular
30 responses could converge over time. These findings suggest a conceptual parallel between the actin
31 cytoskeleton and gene regulatory networks; where the theoretical plasticity of interactions is nearly
32 infinite, yet phenotypes *in vivo* are constrained into a limited subset of practicable configurations.

33 **Keywords**

34 Actin cytoskeleton, F-actin organisation, talin, talin inhibitor, attractor state, plasticity, phenotypic
35 analysis.

36 **Introduction**

37 Our current knowledge of the actin cytoskeleton and its regulatory system – incorporating 6784
38 proteins with actin-related functionality ($> 1/3$ of the annotated human proteome, based on 363
39 distinct gene ontology labels; <http://geneontology.org>) – suggests no clear limits to the organisational
40 plasticity of this complex system. Plasticity in actin organisation physically manifests in the numerous
41 distinct forms and combinations of sub-cellular filamentous actin (F-actin) structure (stress fibres,
42 lamellipodia, filopodia and invadopodia etc) (Burrige and Wittchen, 2013; Lehtimaki et al., 2017;
43 Leijnse et al., 2015; Skau and Waterman, 2015). From a regulatory perspective, the multiplicity of
44 direct actin-binding partners, distal regulatory proteins and impinging signalling pathways that
45 collectively modulate actin organisation (Pollard, 2016) also suggest a high level of organisational
46 diversity. Taken together, this information suggests the potential for virtually unlimited phenotypic
47 plasticity in actin organisation at the cellular scale.

48 Considering the possibility of such wide-ranging plasticity, the diversity of functional demands on the
49 actin cytoskeleton highlight a significant challenge for the evolution and adaptation of this system.
50 How are changes amongst the repertoire of actin-binding and actin-regulatory proteins
51 accommodated without widespread disruption of the cytoskeleton and its numerous parallel
52 functions? A potential clue is provided by the dynamics of a contrasting class of system: gene
53 regulatory networks. Specifically, it has been observed that diverse patterns of genetic mutations
54 (Huang et al., 2009) or mechanistically diverse chemical perturbations (Zhou et al., 2016) may be
55 channelled into strongly convergent patterns of gene expression, suggesting the existence of high-
56 dimensional attractor states (Huang et al., 2005) within the landscape of potential gene regulatory
57 network configurations. Thus, the virtually infinite theoretical plasticity of gene regulatory network
58 states (implying evolutionary instability) is likely constrained into a much more limited subset of
59 practicable configurations. Recent theoretical works now indicate the potential for attractor states to
60 effectively constrain the plasticity of protein signalling and interaction networks (Huang et al., 2017).

61 Here, we have adopted a chemical biology approach to estimate the number of ways in which cells
62 can (re)organize their F-actin cytoskeleton given a large spectrum of perturbations (Bryce et al., 2019).
63 Cells with well-defined, quantifiable actin phenotypes were challenged with 114,400 structurally
64 diverse compounds, previously demonstrated to affect a broad range of cell biological processes. In
65 contrast to both the large number of compounds and large number of actin regulators, we observed
66 a low number of emergent actin phenotypes, each with distinct quantitative features that can be
67 machine-learned. Subsequent selective mechanistic analyses, coupled with temporal analyses of
68 progressive perturbation effects, support the idea that the actin cytoskeleton contains phenotypic
69 attractor states that would be conceptually analogous to those proposed for gene regulatory
70 networks. Taken together, our findings provide an estimate of the degree of organisational plasticity
71 available to the F-actin cytoskeleton, indicating this to be relatively constrained. We suggest that this
72 constraint on plasticity may reflect an emergent process of canalization favouring evolutionarily
73 competent phenotypes and functions within this pivotal biological system.

74 **Results**

75 **Using diverse chemical perturbations to assess the degree of plasticity in F-actin organisation**

76 We challenged a total of 25,619,680 cells using the 114,400 compound WECC structural diversity
77 library (Baell, 2013; Baell and Holloway, 2010), which was established to efficiently sample the
78 chemical space of lead-like compounds with minimal structural similarity (< 85-90%). This approach
79 allowed us to estimate the number of ways in which cells can (re)organize their F-actin cytoskeleton
80 in response to chemical perturbation. This constituted 21 separate biological experiments including
81 more than 320 individual experimental repeats (fifteen to twenty 384-well plates per experiment),
82 each of which included 3 positive and 1 negative control, with these controls replicated 8-fold each
83 per plate. Including both unknown (114,400) and replicated control treatments (>10,000), a total of
84 124,767 experimental conditions were assessed. To read out phenotypic responses we employed
85 quantitative imaging and statistical analyses, with an overview of this approach summarized in Figure

86 1A. As a cell model, SK-N-SH neuroblastoma cells were utilized due to their large, flat morphology and
87 the relative homogeneity of their actin organisation phenotype, which makes drug-induced changes
88 more clearly discernible.

89 **Quantifying F-actin organisation**

90 To observe actin phenotypes, F-actin (phalloidin) and nuclear (Hoechst) markers were assessed via
91 automated spinning-disc confocal imaging (Figure 1B, upper panels). Visual inspection confirmed that
92 compounds from the diversity library induced a variety of distinct actin organisation phenotypes
93 (Figure 2A).

94 Image segmentation (Figure 1B) and analysis extracted 75 quantitative features defining cell
95 morphology, texture as well as properties of actin stress fibres and actin puncta. Measurements from
96 wells with extreme cell numbers or duplicated values were excluded (<10 & >700 cells; 124,343
97 conditions retained; ~200 cells average per condition), removing cytotoxic conditions or overgrown
98 wells. Z-score normalisation of data was performed for each of 74 features (1 excluded due to low
99 variance; features defined in Table S1) relative to all unknown compounds (Birmingham et al., 2009)
100 grouped per experimental batch. This greatly improved data superimposition (Figure S1A, B) and
101 revealed a conserved phenotypic signature across the 74 normalized features (Figure S1C, D) as well
102 as tight alignment of individual feature value distributions across experimental batches (Figure S1E-
103 H).

104 **Estimating F-actin organization phenotype number**

105 Next, we estimated the number of distinct and recurrent phenotypic ‘clusters’ that exist within the
106 complete chemical treatment dataset. To ensure the robustness of this estimation, we combined four
107 complementary methods into a “quadrangulation” strategy (Figure 1C) that progressively narrowed
108 the estimation range to a final approximation of phenotype number. Starting with the possibility that
109 the number of phenotypes may range from two or three up to thousands, method 1 of our

110 quadrangulation strategy involved visual inspection of tens of thousands of images spanning the
111 complete dataset, producing a human expert-guided range estimate for the number of phenotypes
112 that were readily discernible (~15 to ~40). This range estimate was then complimented by method 2;
113 iterative, sub-sampling-based multivariate statistical estimation of phenotypic cluster numbers using
114 hierarchical clustering interpreted via two alternative cluster-detection indices (Dunn's index or SD
115 index) (Figure S2A). Outcomes based on both indices suggested phenotype cluster numbers ranging
116 between ~17 and ~35, supporting the range estimate from visual inspection.

117 The range estimated above was next used to initialise parameterization of dimension reduction and
118 unsupervised clustering approaches for more precise estimations of phenotype number. As detailed
119 below, these approaches were combined to underpin methods 3 and 4 of the quadrangulation
120 strategy introduced above. Dimension reduction was first performed via t-distributed stochastic
121 neighbour embedding (t-SNE) (Van der Maaten and Hinton, 2008) after principle components analysis
122 (PCA) was used to reduce the computational complexity of the data. t-SNE enabled projection of high-
123 dimensional quantitative phenotype observations into a 2D space according to their local similarity
124 (Figure 2B), with unsupervised cluster detection then applied via the OPTICS algorithm to objectively
125 define distinct and recurrent organisational states of F-actin. This revealed an estimate of just 25
126 distinct phenotypes (Figure 2B, phenotypes colour-coded). As schematised in Figure 1C, this result
127 followed extensive exploration of t-SNE tuning parameter (i.e. 'perplexity') values whilst monitoring
128 the trade-off between phenotype number (quadrangulation method 3) (Figure 2C, upper) and positive
129 control 'self-clustering' (quadrangulation method 4) (i.e. representation of homogeneous positive
130 control drug treatments as forming only one major phenotype each; Figure 2C, lower). To further
131 validate this surprisingly low level of F-actin phenotype plasticity, we repeated our entire dimension
132 reduction analysis using the uniform manifold approximation and projection (UMAP) algorithm
133 (McInnes et al., 2018). This produced a recognisably similar projection of the dataset, with OPTICS
134 cluster detection suggesting just 16 distinct phenotypes (Figure 2D, phenotypes colour-coded). Again,
135 this final UMAP projection and phenotype number estimation followed extensive optimisation of the

136 UMAP tuning parameter (i.e. 'nearest neighbour') guided by the trade-off between phenotype
137 number (quadrangulation method 3) (Figure 2E, upper) and positive control 'self-clustering'
138 (quadrangulation method 4) (Figure 2E, lower). The lower phenotype number estimate from UMAP
139 corresponds with recent comparisons of t-SNE and UMAP dimension reduction methods, wherein
140 UMAP tended to identify fewer discernible clusters than t-SNE (Becht et al., 2018). This in part reflects
141 the preservation by UMAP of medium- and long-distance spatial relationships and trajectory / lineage
142 structures that are expected in datasets based on, for example, RNAseq analyses of cell differentiation.
143 Such datasets comport with the progressive manifold assumption (Moon et al., 2018), whereas such
144 progressive manifolds (i.e. trajectories) are not implied by our endpoint analysis of chemical
145 perturbation effects. Hence, we do not here draw interpretations from the distances between
146 phenotype clusters (in either t-SNE or UMAP projections), instead only assessing phenotype number.
147 For this reason, and because t-SNE more accurately preserves local similarities in phenotype (Becht et
148 al., 2018) (by not compromising local *versus* long-distance similarity relationships - thus more faithfully
149 identifying co-clustered compounds that may have similar effects), we continued our analyses using
150 the optimised data projection based on t-SNE dimension reduction.

151 Pairs of images depicting selected cellular phenotypes (Figure 2F) confirm phenotypic homogeneity
152 within each cluster. Individual observations that did not fall into a defined phenotype were excluded
153 from further analysis (1,235 observations excluded; 123,108 observations retained; Figure S2B). To
154 determine which of the 25 t-SNE-estimated phenotypes are spontaneous within the SK-N-SH cell
155 population, i.e. naturally occurring, and which are *bona fide* drug-induced phenotypes, we assessed
156 the frequency of DMSO negative control observations within each phenotype relative to the expected
157 random rate (Figure S2C). This indicated 5 spontaneous and 20 chemically induced phenotypes (Figure
158 S2D). For clarity, the 20 induced phenotypes are shown in Figure S2E.

159 We next sought to characterize the major differences between defined phenotypic clusters. To this
160 end, we first performed machine learning-based forward feature selection using all 74 Z-normalized

161 features, thereby delineating a subset of 15 features that optimally predict phenotype for each
162 observation. The >98% accuracy of the resulting model supports the significance of the 15 feature-
163 subset. Comparison of phenotypes based on these key features reveals a recurring signature that
164 characterizes similarities between most phenotypes while also highlighting specific features that
165 differentiate each (Figure 2G).

166 Visible similarities between cell images within phenotype clusters confirm the efficacy of our
167 clustering strategy. Given that similar image data are clustered by our analysis approach, two key
168 questions remain: **1)** do distinct molecular mechanisms reproducibly generate distinctive F-actin
169 phenotypes? And **2)** do individual phenotypes reflect singular molecular mechanisms?

170 **Known perturbation mechanisms induce reproducible and distinguishable phenotypes**

171 To address question 1, we assessed in detail the clustering of three positive control compounds
172 (jasplakinolide, latrunculin A, TR100) with mechanisms of action towards F-actin that are known and
173 also distinct. Jasplakinolide binds to and stabilizes actin filaments (Bubb et al., 1994), thereby
174 increasing F-actin within the cell relative to the DMSO control (Figure S3A, B). Latrunculin A binds actin
175 monomers, thus inhibiting filament assembly (Spector et al., 1983) and reducing F-actin within the cell
176 (Figure S3C). TR100 binds to tropomyosin isoform Tpm3.1 dimers and is incorporated into actin
177 filaments, thereby accelerating filament depolymerization and reducing organization into stress fibres
178 (Bonello et al., 2016; Janco et al., 2019; Stehn et al., 2013) (Figure S3D). The different mechanisms of
179 these positive control compounds are known to induce F-actin organisation phenotypes that are
180 reproducible, homogeneous and distinct. As such, we expected these conditions to not only self-
181 cluster, but also to cluster separately from each other.

182 As predicted, each of the embedded positive control drugs overwhelmingly clusters within a single
183 distinct phenotype (Figure 3A, shown individually in Figure S3F-I). Specifically, Jasplakinolide,
184 Latrunculin and TR100 induce phenotypes in 91%, 96% and 66% of cases (Figure S3E), and of these

185 induced phenotypes, Jasplakinolide, Latrunculin A and TR100 recurrently fall into specific F-actin
186 phenotypes 3, 4 and 5 in 89%, 95% and 87% of cases, respectively (Figure 3B). This highlights the
187 experimental and analytical reproducibility achieved throughout this study, wherein more than 320
188 individual experimental replicates (i.e. 384-well plates) were processed across 21 independent
189 biological experiments. In contrast to the positive controls, DMSO is broadly distributed, as expected
190 (Figure 3A; Figure S3F). Taken together, these results validate the robustness and sensitivity of the
191 experimental and analytical methods applied herein, since each positive control compound
192 overwhelmingly clustered within a single phenotype (as optimised via the ‘quadrangulation’ strategy,
193 Figure 1C), and these phenotypes are clearly distinguishable. Moreover, comparison of key feature
194 values between these control compounds and phenotype cluster 1 (Figure S3J, the main spontaneous
195 phenotype; large grey cluster in Figure 2B) confirms the expected effects of these control compounds.
196 For instance, latrunculin A reduces actin filament length and intensity whilst increasing actin spot
197 intensity and size (Figure S3J), as observable in Figure S3C. In contrast, TR100 substantially reduces
198 cell area, whilst maintaining long peripheral actin fibres (Figure S3D, J).

199 **Defining the properties of key phenotypic clusters**

200 In total, 1.77% (2003) of unknown compounds were associated with induced phenotypes (Figure S3E),
201 and these were distributed across all 20 induced phenotype clusters (Figure 3C), implying diverse
202 effects and a wide variety of molecular mechanisms. We next focused on understanding the biological
203 differences between key phenotypic clusters. Specifically, we compare phenotype cluster 4
204 (Latrunculin-like phenotype), 5 (TR100-like phenotype) and 9 (the largest unknown induced cluster)
205 wherein we identified significant numbers of co-clustered unknown compounds (cluster 4, 87
206 compounds; cluster 5, 55 compounds; cluster 9, 1166 compounds) (Figure 3C, D). Cell image examples
207 for unknown compounds from each of these phenotype clusters are depicted in Figure 2F.

208 Differences between biological states (here induced by chemical perturbations) can be defined not
209 only by observable changes in phenotypic features, but also by more complex (and less readily

210 discernible) changes in the statistical linkages between these features, which may reflect changes in
211 biological dependencies. To explore such changes in inter-feature linkages, we assessed asymmetries
212 in the mutual information shared between each possible pairing of the 15 machine learning-selected
213 features, using an estimation of the uncertainty coefficient (Figure 3E). This revealed large differences
214 in the number of inter-feature linkages (above a constant minimal threshold) detected in clusters 1
215 and 9 (low connectivity) and clusters 4 and 5 (high connectivity). Comparisons of connectivity changes
216 induced from cluster 1 to clusters 4, 5 and 9 showed that, despite having distinct patterns of
217 phenotypic effect, clusters 4 and 5 reflected extensive and similar alterations in inter-feature
218 connectivity. In contrast, despite a pronounced phenotype, cluster 9 reveals limited effects on inter-
219 feature connectivity.

220 **Do individual phenotypes reflect singular molecular mechanisms?**

221 An important implication of the small number of recurrent phenotypes detected in this study – relative
222 to 114,400 diverse chemical perturbations – is that multiple underlying molecular mechanisms may
223 result in the same phenotypic end-state. To this end, we performed secondary mechanistic analyses
224 of selected unknown compounds drawn from clusters 4, 5 and 9.

225 We first selected the unknown compounds producing latrunculin A-like phenotypes shown in Figure
226 2F (cluster 04), and assessed their mechanistic activities based on two key assays. First, we monitored
227 reductions in cellular F-actin levels using a G:F actin ratio assay (Figure 4A). Mimicking the effects of
228 latrunculin A, unknown compounds L2 and L3 reduced F-actin levels. In contrast, and despite
229 producing a quantitatively equivalent phenotypic end-state, unknown compound L1 had no effect on
230 the G:F actin ratio. To further assess whether L2 and L3 precisely mimic the mechanisms by which
231 Latrunculin impacts the G:F actin ratio, i.e. by inhibiting F-actin assembly, we performed an *in vitro*
232 pyrene actin filament assembly assay to measure F-actin assembly rates (Figure 4B). Neither L2 nor L3
233 directly inhibited F-actin assembly, indicating differences in their precise mechanism of action relative

234 to Latrunculin, again despite their phenotypic similarity. Thus, at least three different mechanisms
235 (latrunculin A, L1, L2/L3) can induce the singular phenotypic end-state defined by cluster 4.

236 We next selected two compounds from the TR100-like phenotypic cluster and used
237 immunofluorescence imaging to determine if Tpm3.1 was removed from F-actin stress fibres. Relative
238 to DMSO-treated control cells (Figure 4C), Tpm3.1 was removed from stress fibres by the compound
239 designated Tr1 (Figure 4D), thus mimicking the effects of TR100. In contrast, the compound designated
240 Tr2 induced a similar actin phenotype without displacing Tpm3.1 from actin filaments (Figure 4E).
241 Thus, once again, equivalent actin phenotypes emerge as a result of distinct underlying mechanisms.

242 Phenotype cluster 9 is the most populous of the induced phenotypes and does not correspond with
243 any of the embedded control drugs (Figure 2B and 3B). Visual inspection (Figure 2F) shows that cluster
244 9 cells are small and round, with thick stress fibres and intense actin puncta. They tend to be isolated
245 rather than in close contact, resulting in low cell density. Interestingly, this phenotype corresponds
246 closely with that induced by overexpression of the focal adhesion protein talin (Figure S4A-C). Talin is
247 critical for integrin activation and mechanically links integrin cytoplasmic tails with F-actin (Klapholz
248 and Brown, 2017; Yao et al., 2016), thereby influencing actin organisation.

249 We hypothesized that compounds found in phenotype cluster 9 may influence talin. Four such
250 compounds (structures in Figure 4F-I; phenotypes Figure S4D-G) were randomly selected for
251 saturation transfer difference (STD) NMR to test for direct talin-binding (Figure 4F-I). Of these, two
252 compounds (designated T1 and T2) bind talin directly and selectively, since they did not also bind
253 another core adhesion component, vinculin (example in Figure S4H). Notably, this expands upon the
254 single talin-binding compound previously identified (Yang et al., 2017). In contrast, compounds
255 designated T3 and T4 did not bind talin despite inducing an indistinguishable phenotype, suggesting
256 possible targeting of a related focal adhesion component. More broadly, these results again confirm
257 the capacity for distinct molecular mechanisms to drive the emergence of singular phenotypic end-
258 states.

259 **Temporal analyses reveal different phenotypic trajectories to the same end-state**

260 We next sought to test whether different compounds that yield the same phenotypic state after 24
261 hours exposure undergo the same phenotypic changes with time or arrive at the 24-hour state via
262 different trajectories. As the phenotypic equivalence of mechanistically distinct perturbations was
263 observed in several instances, and because the limited phenotypic plasticity we observe constitutes a
264 global property of the actin system, we focused on ‘systems-level’ mechanisms that may explain both
265 observations in a coherent manner. Given this perspective, we considered whether the recurrent actin
266 phenotypes we observe might represent particular stable equilibria, or ‘attractor states’, which reflect
267 limited phenotypic options available to the actin cytoskeletal system. This hypothesis was based on
268 two factors. First, such attractor states tend to arise in complex systems composed of extensive, highly
269 inter-dependent networks – characteristics found not only in the context of gene regulation (Huang
270 et al., 2005) but also in the actin regulatory network (Agarwal and Zaidel-Bar, 2018; Senju and
271 Lappalainen, 2018; Steinbacher and Ebnet, 2018). Second, attractor states tend to constitute relatively
272 infrequent points of stable equilibrium within state-space landscapes comprising much larger
273 repertoires of unstable states. Thus, the low phenotypic diversity we have observed after 24 hours of
274 compound exposure mirrors the theoretical view that stable attractors are low-frequency
275 phenomena.

276 Given this reasoning, we investigated whether observed actin phenotypes may actually demarcate
277 stable systems-level attractor states. Specifically, we sought evidence of a third phenomenon
278 predicted by attractor state theory, namely, that distinct transitional states may dynamically converge
279 towards coincident end-states – as has been observed in the behaviour of gene regulatory networks
280 over time (Huang et al., 2005). To test this possibility, we chose two compounds (T1 and T2) that
281 generate equivalent talin-like phenotypes at 24 hours but are also structurally divergent (Figure 4F-
282 G). We mapped actin phenotypes induced by each of these compounds at 12 timepoints post-
283 treatment (1, 5, 15, 30, 45 minutes and 1, 2, 3, 4, 6, 20, 24 hours), enabling comparison of their
284 phenotypic trajectories (Figure 4J).

285 Despite both binding to talin, these compounds induced phenotypes that diverged strongly after just
286 a few minutes of treatment, remaining clearly distinct for several hours (Figure 4J; 4-hour cell images
287 in Figure S5A, left), before converging after ~20 hours of treatment (Figure 4J; 24-hour cell images in
288 Figure S5A, right) (outliers excluded as detailed in Figure S5B-D). These observations support the
289 attractor state hypothesis as an emergent mechanism shaping and constraining phenotypic plasticity
290 within the actin cytoskeletal system.

291 **Discussion**

292 In this study, we estimated the degree of cellular-scale phenotypic plasticity available to the F-actin
293 cytoskeletal system by using a large, structurally diverse library of chemical perturbations to induce a
294 high degree of variability in adaptive responses. This unbiased approach revealed a comparatively low
295 number of (approximately 25) distinct F-actin phenotypes, strongly indicating that F-actin
296 organizational plasticity is constrained to far less than the hundreds or thousands of phenotypes that
297 might have been expected given the large number and diversity of chemical challenges applied
298 (~115k), and the known complexity of the actin regulatory system.

299 Our findings thus support the notion that actin phenotypes reflect a limited set of stable equilibria, or
300 attractor states, in the organisation of the actin system. This is reminiscent of dynamic perturbation
301 responses mapped in high-dimensional analyses of gene regulatory networks (Huang et al., 2009);
302 (Zhou et al., 2016). Crucially, channelling of divergent gene expression profile trajectories towards
303 equivalent end-states is increasingly attributed to the attractor state hypothesis (Huang et al., 2005),
304 with support from Boolean (gene) regulatory network modelling and the broader ‘canalization’
305 concept embodied, for example, in Waddington’s theory of cellular differentiation (Huang, 2012;
306 Waddington, 1942). Notably, these theories draw upon the emergence of a systems-scale ‘logic’ from
307 the highly interconnected and interdependent characteristics of gene regulatory networks.

308 Given the connectivity and interdependence of the actin regulatory network, we suggest that parallels
309 may exist between the emergence of, and constraints on, plasticity in this molecular system.

310 Specifically, mutation-driven changes in actin regulation might be projected to have strongly
311 deleterious consequences, due to the highly interconnected nature of this biological system and its
312 pivotal involvement in so many essential functions. However, our results suggest that by channelling
313 diverse perturbations into a narrow array of recurring attractor states, the actin system achieves an
314 intrinsic buffering capacity that prioritises useful organisation of actin filaments, thereby reducing the
315 impact of deleterious perturbations. Such a buffering capacity may facilitate evolutionary change and
316 diversity at the molecular level while maintaining the integrity of a structural system involved in
317 essentially all cell functions.

318

319 **Acknowledgements:**

320 We thank Dr Galina Schevzov (UNSW) and Dr Jeffrey Stear (UNSW) for helpful discussions, Mike
321 Williams (UNSW) for assistance with data management, and Gary Thompson (Kent) for technical
322 assistance with the NMR data collection. This work was supported by the Australian National Health
323 and Medical Research Council (NHMRC) and from the Kids Cancer Project. B.T.G. and K.B.B are funded
324 by BBSRC grant (BB/N007336/1) and Human Frontiers Science Program grant (RGP00001/2016).

325 **Author Contributions**

326 Conceptualisation: NSB, JRS, ECH, PWG and JGL. Chemical perturbations: TWF, GMA and NSB. Image
327 analysis and data curation: NSB. Statistical analysis: JGL. Target validation: NSB, JGL, KB, ID, CL, BTG
328 and SZ. Software: JGL, YA and LB. Supervision and Funding: NSB, KG, ECH and PWG. Writing – original
329 draft: JGL and NSB. Writing – review and editing: All authors.

330 **Declaration of Interests**

331 PWG and ECH are Directors of TroBio Therapeutics, a company that is commercialising anti-
332 tropomyosin drugs for the treatment of cancer and their labs receive funding from TroBio
333 Therapeutics to evaluate anti-tropomyosin drug candidates.

334 **Figure Legends**

335 **Figure 1.** *Overview of experimental and analytical strategy.* **A)** Flow chart detailing major steps in the
336 phenotypic analysis workflow from cell biology to imaging to statistical analyses. **B)** Raw images of
337 Atto488-phalloidin and Hoechst 33342 staining (upper panels). Image analysis algorithms segment
338 nuclei to seed single cell boundary detection (middle panels). Stress fibres and actin rich puncta are
339 then segmented and measured per cell (bottom panels). Scale bar 50 μm . **C)** "Quadrangulation"
340 Strategy for Phenotype Number Estimation. To objectively estimate the number of distinct
341 phenotypes induced across the 114,400 compounds applied, we combined inferences from 4 distinct
342 methods (see grey boxes). Method 1 involved visual inspection of raw image data, providing a range
343 estimate for the number of visually discernible phenotypes. In method 2, hierarchical clustering was
344 applied using two alternate criteria (the SD index and Dunn's index) to provide additional range
345 estimates for phenotype number (Figure S2A). Both method 1 and 2 suggested that phenotype
346 number lay in the range between ~ 15 and ~ 40 . This range guided subsequent phenotype number
347 estimation based on two alternate dimension reduction techniques (t-SNE [*exploring the tuneable*
348 *'perplexity' parameter-space*] or UMAP [*exploring the tuneable 'nearest neighbours' parameter-*
349 *space*]) combined with cluster (i.e. phenotype) detection (OPTICS algorithm). Using this progressive
350 exploration of the t-SNE and UMAP tuneable parameter-spaces, method 3 seeks the maximum
351 phenotype number and/or the point where this estimate plateaus (Figure 2C (*t-SNE*), 2E (*UMAP*);
352 upper). Method 3 tends to push phenotype number estimates higher (see dashed lines with hollow
353 arrow heads). Conversely, method 4 sets an upper bound on the phenotype number estimate by
354 monitoring "self-clustering" of positive controls (Jasplakinolide, Latrunculin A, TR100). These drugs are
355 known to induce relatively homogeneous phenotypes, providing a ground-truth expectation that
356 these treatments should predominantly "self-cluster" into a single phenotype. "Fragmentation" of any
357 of these controls into multiple phenotypes (resulting in reduced self-clustering) therefore implies
358 over-clustering/over-fitting, i.e. an excessive estimate of phenotype number (Figure 2C (*t-SNE*), 2E
359 (*UMAP*); lower). Thus, method 4 tends to constrain phenotype number estimates (see dashed lines

360 with solid arrow heads). When combined, the trade-off between method 3 and 4 defines a final
361 optimised phenotype number estimate (using either t-SNE or UMAP dimension reduction).
362 Significantly, both UMAP (~16 phenotypes) and t-SNE (~25 phenotypes) suggest the emergence of a
363 surprisingly low number of distinct phenotypes.

364

365 **Figure 2.** *Assessing the diversity of F-actin organisation phenotypes using unbiased chemical*
366 *perturbations. A)* Example images of the diverse F-actin organisation phenotypes induced by chemical
367 perturbations. Scale bar 50 μm . **B)** Scatter plot of observations (123,108 observations, $n = 22$
368 independent experiments) distributed according to t-SNE dimension reduction (t-SNE tuneable
369 parameter 'perplexity' = 60) with 25 distinct phenotype clusters (colour-coded) defined by
370 unsupervised clustering via the OPTICS algorithm. **C)** To select the optimal t-SNE projection, 17
371 perplexity values were tested with 11 random seeding-replicates per value (187 total t-SNE
372 projections) as part of the 'quadrangulation strategy' (described in Figure 1C) for t-SNE projection
373 optimisation. Monitoring of changes in detected phenotype number (Y-axis, *upper panel*) and positive
374 control 'self-clustering' (Y-axis, *lower panel*; Jasplakinolide, aqua; Latrunculin, yellow; TR100, pink)
375 identified the optimal perplexity value (60, as used in B; dashed vertical line; X-axes). Smoothed means
376 (thin solid lines), 95% confidence intervals of smoothed means (pale envelopes) and median values
377 (dashed lines) are shown. **D)** Scatter plot of observations distributed according to UMAP dimension
378 reduction (UMAP tuneable parameter 'nearest neighbour' = 21) with 16 distinct phenotype clusters
379 (colour-coded) defined by unsupervised clustering via the OPTICS algorithm. **E)** To select the optimal
380 UMAP projection, 14 nearest neighbour values were tested with 11 random seeding-replicates per
381 value (154 total UMAP projections) as part of the 'quadrangulation strategy' (described in Figure 1C)
382 for UMAP projection optimisation. Monitoring of changes in predicted phenotype number (*upper*
383 *panel*, Y-axis) and positive control 'self-clustering' (*lower panel*, Y-axis; Jasplakinolide, green;
384 Latrunculin, red; TR100, orange) allowed identification of the optimal nearest neighbour value (21, as

385 used in D; dashed vertical line; X-axes). Smoothed means (thin solid lines), 95% confidence intervals
386 of smoothed means (pale envelopes) and median values (dashed lines) are shown. **F)** Example screen
387 images of phenotypes induced by two unknown compounds from each selected cluster. Scale bar 50
388 μm . **G)** Parallel coordinates plot depicting similarities and differences between all 25 phenotype
389 clusters (colour-coded as in D) across 15 key feature values. Key features determined by forward
390 feature selection based on random forest machine learning.

391

392 **Figure 3.** *Distinct clustering of compounds confirms robustness and sensitivity of the phenotypic*
393 *analyses and allows comparative analyses of feature values and inter-feature relationships to highlight*
394 *specific differences between major phenotypes. A)* 2D t-SNE plot showing 123,108 observations ($n =$
395 22 independent experiments) highlighting the distribution of the 4 control compounds: DMSO (pink);
396 Jasplakinolide (yellow); Latrunculin A (red); TR100 (green). **B)** Sunburst plot showing how control or
397 unknown compounds map to drug-induced cluster phenotypes. **C)** Sunburst plot showing the number
398 of unknown compounds in induced phenotype clusters. **D)** Enlarged views of clusters 4, 5 and 9 with
399 co-clustered unknown compounds denoted as black dots and the number of unknown compounds
400 listed. E) Upper row; for each of 4 major phenotypic clusters (1, 4, 5, 9), networks depict the wiring of
401 information theoretic dependencies between pairs of key features based on calculation of uncertainty
402 coefficients. Arrows indicate the direction of an inferred dependency, based on the mutual
403 information between each feature pairing, corrected for asymmetries in the entropy of each feature.
404 The relative strength of dependencies is coded by line thickness and colour (yellow, weak; red, strong).
405 Lower row; networks depict plasticity in uncertainty coefficient dependencies between each feature
406 pair based on comparison of phenotypic clusters 4, 5 or 9 to cluster 1 (the main non-responsive
407 phenotype). This highlights relationships that are 'gained' (present in phenotype 4, 5 or 9 but not in
408 1; purple), versus relationships that are 'lost' (present in phenotype 1 but not in 4, 5 or 9; cyan).

409

410 **Figure 4.** *Compounds producing co-clustered phenotypes can have distinct mechanisms of action.* **A)**
411 Western blot of a representative G:F actin assay (3 independent experiments) probed with total actin
412 antibody. Changes in actin composition between G-actin (G) and F-actin (F) for 3 compounds identified
413 from the Latrunculin-like cluster 4 as well as the positive control Latrunculin A and vehicle control
414 DMSO are shown. **B)** Representative line graph (3 independent experiments) of pyrene actin filament
415 assembly in response to Latrunculin-like compounds L2 and L3, compared with the positive control
416 Latrunculin and vehicle control DMSO. **C-E)** Representative widefield fluorescent images of SK-N-SH
417 cells immunostained with the γ 9d antibody that detects Tpm3.1. Cells were treated with DMSO (**C**),
418 or two compounds from cluster 5 that had differential effects on Tpm3.1 incorporation into stress
419 fibres (**D,E**), scale bars C-E 20 μ m. **(F-I)**. Talin binding assay. Representative NMR spectra of compounds
420 T1-T4 (blue lines) and STD-NMR spectra (red lines) of compounds T1-T4 in the presence of full length
421 talin. Chemical structures of compounds T1 (PubChem CID 42913180), T2 (PubChem CID 850363), T3
422 (PubChem CID 3351420) and T4 (PubChem CID 1211816) are shown inset. **J)** Comparison of time-
423 resolved phenotypic trajectories in t-SNE-space for cells treated with T1 (10 μ M, duplicate wells; small
424 yellow to large red dots indicative of treatment time from 1 minute to 24 hours) vs T2 (10 μ M,
425 duplicate wells; small cyan to large dark blue dots indicative of treatment time from 1 minute to 24
426 hours). Bezier-fitted lines (T1 – dark red; T2 – purple; arrows indicate the direction of time) highlight
427 the equivalence of initial phenotypes (adjacent to negative controls – grey dots). Trajectories rapidly
428 diverge in phenotypic space during the initial hours of treatment before converging again at 20 and
429 24 hours. **K)** Convergent phenotypic responses; a schematic summary of evidence for an evolutionary
430 buffering capacity in actin phenotype control in the face of diverse chemical challenges. By challenging
431 the actin cytoskeleton to respond to an overwhelming diversity of chemical perturbations ('High
432 Perturbation Diversity; drug 'perturbation diversity' hierarchy illustrative only), we have revealed how
433 such diverse challenges are channelled into a limited number of organisational phenotypes ('Low
434 Phenotypic Diversity'; calculated 'phenotypic diversity' hierarchy shown, see also Figure S6). This
435 implies that numerous molecular mechanisms of action may translate into singular phenotypic

436 outcomes, a suggestion confirmed by comparisons of the mechanisms-of-action within several pairs
437 of chemical compounds drawn equivalent phenotypic clusters ('Distinct mechanisms with same
438 phenotype'). This convergence of mechanistic diversity into phenotypic similarity suggests that
439 recurrent actin phenotypes may constitute attractor states within the broader actin phenotypic
440 landscape. This attractor state hypothesis is supported by the final convergence of initially divergent
441 phenotypic trajectories, as detailed in Figure 4J.

442 **References**

- 443 Agarwal, P., and Zaidel-Bar, R. (2018). Principles of Actomyosin Regulation In Vivo. Trends in cell
444 biology.
- 445 Ankerst, M., Breunig, M.M., Kriegel, H.-P., and Sander, R. (1999). OPTICS: ordering points to identify
446 the clustering structure. SIGMOD Rec 28, 49-60.
- 447 Baell, J.B. (2013). Broad coverage of commercially available lead-like screening space with fewer
448 than 350,000 compounds. Journal of chemical information and modeling 53, 39-55.
- 449 Baell, J.B., and Holloway, G.A. (2010). New substructure filters for removal of pan assay interference
450 compounds (PAINS) from screening libraries and for their exclusion in bioassays. Journal of medicinal
451 chemistry 53, 2719-2740.
- 452 Becht, E., Dutertre, C.-A., Kwok, I.W.H., Ng, L.G., Ginhoux, F., and Newell, E.W. (2018). Evaluation of
453 UMAP as an alternative to t-SNE for single-cell data. bioRxiv, 298430.
- 454 Berthold, M.R., Cebron, N., Dill, F., Gabriel, T.R., Kötter, T., Meinl, T., Ohl, P., Sieb, C., Thiel, K., and
455 Wiswedel, B. (2008). KNIME: The Konstanz Information Miner (Berlin, Heidelberg: Springer Berlin
456 Heidelberg).
- 457 Biedler, J.L., Helson, L., and Spengler, B.A. (1973). Morphology and growth, tumorigenicity, and
458 cytogenetics of human neuroblastoma cells in continuous culture. Cancer research 33, 2643-2652.
- 459 Birmingham, A., Selfors, L.M., Forster, T., Wrobel, D., Kennedy, C.J., Shanks, E., Santoyo-Lopez, J.,
460 Dunican, D.J., Long, A., Kelleher, D., *et al.* (2009). Statistical methods for analysis of high-throughput
461 RNA interference screens. Nature methods 6, 569.
- 462 Bonello, T.T., Janco, M., Hook, J., Byun, A., Appaduray, M., Dedova, I., Hitchcock-DeGregori, S.,
463 Hardeman, E.C., Stehn, J.R., Bocking, T., *et al.* (2016). A small molecule inhibitor of tropomyosin
464 dissociates actin binding from tropomyosin-directed regulation of actin dynamics. Sci Rep 6, 19816.
- 465 Bryce, N.S., Hardeman, E.C., Gunning, P.W., and Lock, J.G. (2019). Chemical biology approaches
466 targeting the actin cytoskeleton through phenotypic screening. Curr Opin Chem Biol 51, 40-47.
- 467 Bubb, M.R., Senderowicz, A.M., Sausville, E.A., Duncan, K.L., and Korn, E.D. (1994). Jasplakinolide, a
468 cytotoxic natural product, induces actin polymerization and competitively inhibits the binding of
469 phalloidin to F-actin. The Journal of biological chemistry 269, 14869-14871.
- 470 BurrIDGE, K., and Wittchen, E.S. (2013). The tension mounts: stress fibers as force-generating
471 mechanotransducers. The Journal of cell biology 200, 9-19.
- 472 Charrad, M., Ghazzali, N., Boiteau, V., and Niknafs, A. (2014). NbClust: An R Package for Determining
473 the Relevant Number of Clusters in a Data Set. 2014 61, 36.
- 474 Cleary, P.W., Tomas, D., Bolger, M., Hetherington, L., Rusinski, C., and Watkins, D. (2015). Using
475 Workspace to automate workflow processes for modelling and simulation in engineering. Paper
476 presented at: MODSIM2015, 21st International Congress on Modelling and Simulation.
- 477 Dunn, J.C. (1974). Well-Separated Clusters and Optimal Fuzzy Partitions. Journal of Cybernetics 4, 95-
478 104.

479 Hahsler, M., and Peißenbrock, M. (2017). dbSCAN: Density Based Clustering of Applications with
480 Noise (DBSCAN) and Related Algorithms. R package version 1.1-1. .

481 Halkidi, M., Vazirgiannis, M., and Batistakis, Y. (2000). Quality Scheme Assessment in the Clustering
482 Process, Vol 1910.

483 Huang, S. (2012). The molecular and mathematical basis of Waddington's epigenetic landscape: a
484 framework for post-Darwinian biology? *Bioessays* 34, 149-157.

485 Huang, S., Eichler, G., Bar-Yam, Y., and Ingber, D.E. (2005). Cell fates as high-dimensional attractor
486 states of a complex gene regulatory network. *Physical review letters* 94, 128701.

487 Huang, S., Ernberg, I., and Kauffman, S. (2009). Cancer attractors: a systems view of tumors from a
488 gene network dynamics and developmental perspective. *Semin Cell Dev Biol* 20, 869-876.

489 Huang, S., Li, F., Zhou, J.X., and Qian, H. (2017). Processes on the emergent landscapes of
490 biochemical reaction networks and heterogeneous cell population dynamics: differentiation in living
491 matters. *Journal of The Royal Society Interface* 14.

492 Inc., P.T. (2015). Collaborative data science (Montréal, QC: Plotly Technologies Inc.).

493 Janco, M., Rynkiewicz, M.J., Li, L., Hook, J., Eiffe, E., Ghosh, A., Bocking, T., Lehman, W.J., Hardeman,
494 E.C., and Gunning, P.W. (2019). Molecular integration of the anti-tropomyosin compound ATM-3507
495 into the coiled coil overlap region of the cancer-associated Tpm3.1. *Sci Rep* 9, 11262.

496 Klapholz, B., and Brown, N.H. (2017). Talin - the master of integrin adhesions. *Journal of cell science*
497 130, 2435-2446.

498 Krijthe, J.H. (2015). {Rtsne}: T-Distributed Stochastic Neighbor Embedding using Barnes-Hut
499 Implementation.

500 Lehtimäki, J., Hakala, M., and Lappalainen, P. (2017). Actin Filament Structures in Migrating Cells.
501 *Handbook of experimental pharmacology* 235, 123-152.

502 Leijnse, N., Oddershede, L.B., and Bendix, P.M. (2015). An updated look at actin dynamics in
503 filopodia. *Cytoskeleton (Hoboken, NJ)* 72, 71-79.

504 Malo, N., Hanley, J.A., Cerquozzi, S., Pelletier, J., and Nadon, R. (2006). Statistical practice in high-
505 throughput screening data analysis. *Nat Biotechnol* 24, 167-175.

506 McInnes, L., Healy, J., and Melville, J. (2018). Umap: Uniform manifold approximation and projection
507 for dimension reduction. *arXiv preprint arXiv:180203426*.

508 Moon, K.R., Stanley, J.S., Burkhardt, D., van Dijk, D., Wolf, G., and Krishnaswamy, S. (2018). Manifold
509 learning-based methods for analyzing single-cell RNA-sequencing data. *Current Opinion in Systems*
510 *Biology* 7, 36-46.

511 Murtagh, F., and Legendre, P. (2014). Ward's Hierarchical Agglomerative Clustering Method: Which
512 Algorithms Implement Ward's Criterion? *Journal of Classification* 31, 274-295.

513 Pollard, T.D. (2016). Actin and Actin-Binding Proteins. *Cold Spring Harbor perspectives in biology* 8.

514 Schevzov, G., Whittaker, S.P., Fath, T., Lin, J.J., and Gunning, P.W. (2011). Tropomyosin isoforms and
515 reagents. *Bioarchitecture* 1, 135-164.

516 Senju, Y., and Lappalainen, P. (2018). Regulation of actin dynamics by PI(4,5)P2 in cell migration and
517 endocytosis. *Current opinion in cell biology* 56, 7-13.

518 Shaner, N.C., Lambert, G.G., Chammas, A., Ni, Y., Cranfill, P.J., Baird, M.A., Sell, B.R., Allen, J.R., Day,
519 R.N., Israelsson, M., *et al.* (2013). A bright monomeric green fluorescent protein derived from
520 *Branchiostoma lanceolatum*. *Nature methods* 10, 407-409.

521 Skau, C.T., and Waterman, C.M. (2015). Specification of Architecture and Function of Actin
522 Structures by Actin Nucleation Factors. *Annual review of biophysics* 44, 285-310.

523 Spector, I., Shochet, N.R., Kashman, Y., and Groweiss, A. (1983). Latrunculin: novel marine toxins
524 that disrupt microfilament organization in cultured cells. *Science (New York, NY)* 219, 493-495.

525 Stehn, J.R., Haass, N.K., Bonello, T., Desouza, M., Kottyan, G., Treutlein, H., Zeng, J., Nascimento,
526 P.R., Sequeira, V.B., Butler, T.L., *et al.* (2013). A novel class of anticancer compounds targets the actin
527 cytoskeleton in tumor cells. *Cancer research* 73, 5169-5182.

528 Steinbacher, T., and Ebneth, K. (2018). The regulation of junctional actin dynamics by cell adhesion
529 receptors. *Histochemistry and cell biology* 150, 341-350.

530 Team, R.C. (2014). R: A language and environment for statistical computing. R Foundation for
531 Statistical Computing, Vienna, Austria.
532 Ulyanov, D. (2016). Multicore-TSNE (Github).
533 van der Maaten, L. (2014). Accelerating t-SNE using Tree-Based Algorithms. *Journal of Machine*
534 *Learning Research* 15, 3221-3245.
535 Van der Maaten, L., and Hinton, G.E. (2008). Visualizing High-Dimensional Data Using t-SNE. . *Journal*
536 *of Machine Learning Research* 9, 2579-2605.
537 Vindin, H., Bischof, L., Gunning, P., and Stehn, J. (2014). Validation of an algorithm to quantify
538 changes in actin cytoskeletal organization. *J Biomol Screen* 19, 354-368.
539 Waddington, C.H. (1942). Canalization of development and the inheritance of acquired characters.
540 *Nature* 150, 563.
541 Ward, J.H. (1963). Hierarchical Grouping to Optimize an Objective Function. *Journal of the American*
542 *Statistical Association* 58, 236-244.
543 Wickham, H. (2009). *ggplot2: Elegant Graphics for Data Analysis* (New York: Springer-Verlag).
544 Yang, C., Kwon, S., Kim, S.J., Jeong, M., Park, J.Y., Park, D., Hong, S.J., Jung, J.W., and Kim, C. (2017).
545 Identification of Indothiazinone as a Natural Antiplatelet Agent. *Chemical biology & drug design*.
546 Yao, M., Goult, B.T., Klapholz, B., Hu, X., Toseland, C.P., Guo, Y., Cong, P., Sheetz, M.P., and Yan, J.
547 (2016). The mechanical response of talin. *Nature communications* 7, 11966.
548 Zhou, J.X., Isik, Z., Xiao, C., Rubin, I., Kauffman, S.A., Schroeder, M., and Huang, S. (2016). Systematic
549 drug perturbations on cancer cells reveal diverse exit paths from proliferative state. *Oncotarget* 7,
550 7415-7425.

551

552 **STAR Methods**

553 **Contact for reagent and resource sharing**

554 Further information and requests for resources and reagents should be directed to and will be
555 fulfilled by the Lead Contact, Dr John Lock (john.lock@unsw.edu.au) or else by Prof. Peter Gunning
556 (p.gunning@unsw.edu.au). This study did not generate any unique reagents. There are restrictions
557 to the availability of compound identifiers for commercial reasons.

558 **Experimental model**

559 Human, female, SK-N-SH neuroblastoma cells (Biedler et al., 1973) were cultured in Dulbecco's
560 Modified Eagle Medium (DMEM) plus 10% fetal bovine serum (Invitrogen) in a humidified
561 environment at 37 °C with 5 % CO₂. Cells were confirmed to be Mycoplasma free with tests performed
562 using the PCR Mycoplasma Test kit (AppliChem GmbH) as per manufacturer's instructions. Cells were
563 transfected with pmNeonGreen-talin (a gift from Nathan Shaner and Jiwu Wang) (Shaner et al., 2013)
564 using Lipofectamine LTX (Invitrogen).

565 **Method details**

566 **Unbiased chemical perturbations**

567 Unbiased chemical perturbations were conducted using the 114,400 compound WECC diversity library
568 (Baell, 2013; Baell and Holloway, 2010). SK-N-SH cells were seeded at a density of 1800 cells/well into
569 384-well ViewPlates (Perkin Elmer) using a Multidrop 384 (Thermo) liquid dispenser and incubated at
570 37°C for 18 h. Library compounds and negative (vehicle only; DMSO) and phenotype-specific positive
571 controls (8 µM TR100, 40 nM Jasplakinolide, 250 nM Latrunculin A) were dispensed to assay plates
572 (100 nL; each control replicated 8 times per plate) using a Janus liquid handling robot (Perkin Elmer)
573 equipped with a 384-well pintool in a cell::explorer automated workstation (Perkin Elmer). A total of
574 124,767 experimental conditions were assayed over n = 22 independent experiments. Each library
575 compound was applied as a chemical perturbation at a single fixed concentration of 10 µM. Following
576 24 h drug exposure cells were fixed by addition of 16% paraformaldehyde (PFA) (ProSciTech) for 30

577 min at room temperature using a Multidrop Combi liquid dispenser (Thermo Scientific). Cells were
578 washed twice with PBS using a Biotek Elx405 plate washer

579 **Cell Labelling, Imaging and Image Analysis**

580 Cells were permeabilised and stained concurrently with a solution of phalloidin 488-atto (1:1000, Atto-
581 Tec GmbH), Hoechst 33342 (1:10000, ThermoFisher) and Triton X-100 (0.1%, Sigma) in PBS in the dark
582 for 1 h. Stain solution was dispensed using a Janus liquid handling robot. Cells were then washed twice
583 with PBS prior to imaging. Images were acquired on an Opera LX high-content imaging system
584 equipped with spinning disk confocal optics, using a 20X air objective (numerical aperture 0.45). A
585 total of 8 fields of view were acquired for each well using two excitation sources, a 200mW 488nm
586 solid state laser (320ms exposure) and a Xenon UV lamp (40ms exposure). Each image was captured
587 with a 12-bit high QE CCD camera and no pixel binning was applied to the images. Image data was
588 then uploaded to both the Columbus data storage and analysis server (Perkin Elmer) or departmental
589 servers for analysis via the Columbus or Workspace programs respectively (details provided in
590 methods sections quantification and statistical analysis: image analysis).

591 **G-actin:F-Actin assay**

592 Each of 3 independent experiments was performed as follows: 1.5×10^6 cells were plated on 10 cm
593 dishes and incubated overnight. After treatment with DMSO or 25 μ M of compound for 24 h, the cells
594 were harvested and processed using the G-actin/F-actin *In Vivo* Assay Biochem Kit (Cytoskeleton) as
595 per the manufacturer's protocol. The positive control of 5 μ M Latrunculin A was incubated with cells
596 for 1 h before sample processing. The G-actin and F-actin fractions were run on 10% SDS-PAGE gels
597 and transferred for Western blotting onto a PVDF membrane using the Trans-Blot Turbo (Bio-Rad)
598 transfer system. Actin was detected using the C4 total actin antibody and the blot developed with
599 Luminata Crescendo Western HRP substrate (Merck) and imaged on a ChemiDoc MP imaging system
600 (Bio-Rad).

601 **Tpm3.1 localisation**

602 Each of 3 independent experiments was performed as follows: 2×10^5 cells were plated onto a
603 coverslip in a 6 well plate and incubated at 37°C for 18 h. The cells were then treated with 10 μ M of
604 compound for 24 h. The cells were fixed with 4% paraformaldehyde and permeabilized with ice cold
605 methanol, then blocked with 2% FBS for 1 h. Tpm3.1 was detected using the γ 9d antibody (Schevzov
606 et al., 2011) and a Alexa488-labelled secondary antibody. Widefield fluorescent images were taken
607 on a Zeiss Axioskop40 using a Plan Apochromat 63X 1.4 Oil DIC lens with a Axiocam 506 mono
608 camera and ZEN 2.5 (blue edition) software (Zeiss).

609 **Expression and purification of full length talin1**

610 *E. coli* BL21(DE3) were transformed with a pet21a plasmid containing full-length mouse Talin1 (FL-
611 mTalin1) with a non-cleavable C-terminal His-tag. A single colony was used to inoculate a 5 ml
612 overnight LB+ampicillin (100 μ g/ml) culture that was then added to 500 ml LB+ampicillin and grown
613 at 37°C to a density (OD_{600}) of 0.4. Protein expression was induced by addition of 200 μ M IPTG, at 37°C
614 for 3 h. Harvested cells were resuspended in 50 mM Tris pH 7.5, 500 mM NaCl, 10 mM imidazole, 5mM
615 phenylmethylsulfonyl fluoride (PMSF) and lysed by sonication. Clarified cell lysate was bound to 1 ml
616 Ni-NTA resin using a batch method. FL-mTalin1 was eluted from the Ni-NTA resin in 2 ml of 50 mM
617 Tris pH 7.5, 500 mM NaCl, 150 mM imidazole, 5 mM PMSF. The purified talin was dialysed into 10 mM
618 Phosphate pH 7.4, 75 mM NaCl, 2 mM DTT.

619 **Saturation Transfer Difference Nuclear Magnetic Resonance (STD-NMR)**

620 All NMR experiments were carried out at 25°C, in 10 mM sodium phosphate pH 7.4, 75 mM NaCl, 2
621 mM DTT, 5% (v/v) D₂O using a Bruker AVANCE III 600 MHz spectrometer equipped with CryoProbe.
622 600 μ l FL-mTalin1 was prepared at a concentration of 1.5 μ M, in 5 mm NMR sample tubes. TA Drug
623 compounds (50 mM Stocks in DMSO) were added to FL-mTalin1 at a final concentration of 1.5 mM, 3
624 % DMSO was added to FL-mTalin1 for the control sample. A 1D reference spectrum was collected of
625 all compounds at a concentration of 1.5 mM. All spectra were processed using Topspin.

626 STD-NMR spectra were acquired with 32k data points and 700 scans. The protein was irradiated at -1
627 ppm (on-resonance) and -30 ppm (off-resonance) with a train of Gaussian shaped pulses (50 ms). The
628 saturation time used in the STD experiments was 2 s. STD-NMR experiments were optimized on ligand-
629 only samples to ensure that the irradiation at the selected frequency for on-resonance scan did not
630 affect the ligand. The protein resonances were suppressed with a 30 ms spin-lock pulse. The final
631 saturation difference spectra were obtained by subtraction of the on-resonance spectra from the off-
632 resonance spectra.

633 **Pyrene assay**

634 Each of 3 independent experiments was performed as follows: Pyrene actin was purchased from
635 Hypermol (Bielefeld, Germany) and diluted to a 1 mg/mL (24 μ M) stock solution. Before use,
636 spontaneously formed actin aggregates were removed by ultracentrifugation for 1 h at 40,000 rpm
637 and 4 °C. 50 μ l samples for the pyrene assay consisted of: 30 μ l H₂O, 10 μ l MgCl₂ (10 mM), 5 μ l F-actin
638 Buffer (100 mM Imidazole-Cl pH 7.4, 10 mM ATP, Hypermol, Germany), as well as 5 μ l DMSO
639 (containing the indicated concentrations of the respective compound). 10 μ l pyrene actin (24 μ M)
640 were rapidly added to start polymerization. Pyrene fluorescence was monitored every 20 s over 1 h in
641 a 96-well fluorescence plate reader (Tecan) with 360 nm excitation and emission at 400 nm in
642 duplicate.

643 **Compounds**

644 Individual compounds for secondary analyses were sourced through Molport (Latvia). Stock solutions
645 of 50 mM in DMSO were aliquoted for single use and stored at -20°C. TR100 (GVKBio, India),
646 Jasplakinolide (Cayman Chemical) and Latrunculin A (Adipogen Life Sciences).

647 **Quantification and statistical analysis**

648 **Image analysis**

649 Cell morphometry and textural properties were measured using a custom workflow in Columbus
650 (Perkin Elmer). Image analysis was developed and carried out within CSIRO's Workspace software

651 platform (Cleary et al., 2015). Workspace is a cross-platform framework for constructing workflows in
652 a graphic drag-drop editor for a range of applications, including image analysis. Workspace’s flexible
653 architecture allows users to connect their own specialized plug-ins to the framework. Our custom
654 cellular analysis workflow combined operations such as nucleus detection, cell detection and filament
655 detection from Image Analysis plug-in developed by CSIRO’s Quantitative Imaging. In addition to the
656 filament detection previously described (Vindin et al., 2014) the updated algorithm finds and
657 quantifies punctate (“dot-like”) structures within each cell, using a dot detector. The punctate
658 structures are detected relative to the background intensity. The dots, or regions of peak intensity,
659 are detected for a range of dot diameters. The peaks are thresholded on basis of relative (i.e. above
660 background) and absolute intensity. Parameters were initially optimized, then kept constant across all
661 chemical perturbations, in order to achieve measurements that correlated closely with actin
662 organisation. This was confirmed by eye using an overlay of software output with the original image.

663 **Data and Code Availability Statement**

664 The dataset and code generated during this study are available at Data Dryad,
665 <https://doi.org/10.5061/dryad.1cg2dq2>

666 **Software and general data visualization**

667 Data derived from image quantification were statistically analysed and visualized using Knime
668 (Berthold et al., 2008) with R (Team, 2014) integration. Data were primarily visualized using the R
669 packages “ggplot2” (Wickham, 2009) and “plotly” (Inc., 2015). Sunburst plots were generated using
670 the D3.js implementation in Knime. Workflow schematics were generated using Lucidchart (Lucid
671 Software Inc.).

672 **Data import and initial filtering**

673 Quantitative data derived from 328 individual 384-well plates were first filtered to remove missing
674 values (124,767 observations retained). Data were further filtered to remove conditions with less than

675 10 or more than 700 cell measurements as well as duplicated values, leaving 124,343 conditions
676 characterized by 75 measured features.

677 **Normalization**

678 Z-score normalization of data was performed per measured feature (1 feature removed due to low
679 variance) using robust statistics (median and median absolute deviation; MAD) (Malo et al., 2006)
680 describing the entire population of unknown drugs grouped per experimental date (25 dates). The
681 unknown drug Treatment population was a more effective reference for normalization than the DMSO
682 negative control because the Treatment population was orders of magnitude larger and because the
683 majority of these drugs induced no phenotype (~90%) (Birmingham et al., 2009). Normalization using
684 the Treatment population therefore achieved the best superimposition of data, enabling detection of
685 distinct phenotypes as opposed to inter-experimental variation.

686 **Cluster Number Estimation**

687 The number of data clusters (potential phenotypes) was estimated using the R package “NbClust”
688 (Charrad et al., 2014) based on Manhattan distances as a proximity measure and using Ward’s
689 agglomerative hierarchical clustering method (Ward, 1963) to minimize total within-cluster-distances,
690 including a correction criterion where dissimilarities (distances) are squared before iteration updating
691 (Murtagh and Legendre, 2014). Two alternative indices were used to finally estimate the number of
692 clusters: Dunn’s validity index, based on optimizing the distance between clusters *versus* the diameter
693 of clusters (Dunn, 1974) and; the SD validity index, based on optimizing the total separation of clusters
694 *versus* the average scattering of clusters (Halkidi et al., 2000). This procedure was performed using a
695 random sampling of approximately 10% of the dataset (12,000 observations) including all 74 Z-
696 normalized quantitative features, and was repeated 20 times. The mean estimates (~24 clusters,
697 Dunn’s index; ~28 clusters, SD index) were used to guide parameterization of subsequent dimension
698 reduction and unsupervised clustering steps.

699 **t-SNE Dimension Reduction**

700 To limit data set complexity whilst retaining maximal information, principal components analysis (PCA)
701 was performed prior to t-distributed stochastic neighbour embedding (t-SNE)-based dimension
702 reduction. PCA was performed using all 74 Z-normalized quantitative features and parameterized to
703 retain no less than 98% of total data set variance, resulting in the generation of 26 orthogonal principal
704 components. t-SNE-based dimension reduction to 2 dimensions was then performed via the
705 accelerated Barnes-Hut implementation (van der Maaten, 2014) using the R package “Rtsne” (Krijthe,
706 2015). As described in Figure 1C and Figure 2C, a quadrangulation strategy was used to guide
707 optimisation of the main t-SNE tuning parameter, perplexity, leading to a final selected value of 60. As
708 part of the quadrangulation strategy, 17 perplexity parameters values were tested, with 11 random
709 seeding states replicated at each perplexity value, resulting in 187 distinct t-SNE projections.
710 Performed directly within R, this process was accelerated through use of the ‘Rtsne.multicore’ package
711 available from <https://github.com/DmitryUlyanov/Multicore-TSNE> (Ulyanov, 2016).

712 **UMAP Dimension Reduction**

713 To limit data set complexity whilst retaining maximal information, principal components analysis (PCA)
714 was performed prior uniform manifold approximation and projection (UMAP)-based dimension
715 reduction (McInnes et al., 2018). As with t-SNE, PCA was first performed using all 74 Z-normalized
716 quantitative features and parameterized to retain no less than 98% of total data set variance, resulting
717 in the generation of 26 orthogonal principal components. UMAP-based dimension reduction to 2
718 dimensions was then performed directly in R via the ‘umap’ package. As described in Figure 1C and
719 Figure 2E, a quadrangulation strategy was used to guide optimisation of the main UMAP tuning
720 parameter, nearest neighbour, leading to a final selected value of 21. As part of the quadrangulation
721 strategy, 14 nearest neighbour parameter values were tested, with 11 random seeding states
722 replicated at each nearest neighbour value, resulting in 154 distinct UMAP projections.

723 **OPTICS Observation Clustering**

724 To define robust and recurrent phenotypes based on observation clustering within 2D t-SNE or UMAP
725 spaces, the rapid OPTICS (ordering points to identify the clustering structure) (Ankerst et al., 1999)
726 unsupervised clustering algorithm was employed via the R package “dbscan” (Hahsler and
727 Peißenbrock, 2017). For clustering in the optimised t-SNE space, epsilon (0.3), minimum number of
728 points (18) and cluster threshold (i.e. `eps_cl`; 0.3) values were selected based results of the
729 quadrangulation strategy (Figure 1C) for t-SNE analysis. 25 observation clusters (phenotypes) were
730 thus defined, with 1,235 non-clustered observations excluded, leaving 123,108 observations retained.
731 This exclusionary approach to non-clustered observations was utilized so as to focus on robust and
732 recurring phenotypes, rather than potentially unique (or noise-induced) perturbation-effects. For
733 clustering in the optimised UMAP space, epsilon (0.15), minimum number of points (18) and cluster
734 threshold (i.e. `eps_cl`; 0.15) values were selected based results of the quadrangulation strategy (Figure
735 1C) for UMAP analysis.

736 **Supervised Feature Selection**

737 To identify a limited set of (15) features that are maximally informative about differences between
738 phenotypes, we applied Forward Feature Selection in combination with Random Forest machine
739 learning-based prediction of phenotype (cluster) membership for 123,108 observations defined by all
740 74 Z-score normalized features. Using Knime, the Random Forest model was optimized by iterating
741 over randomly partitioned data (20% for learning in presence of phenotype membership data; 80%
742 for phenotype prediction in absence of phenotype membership data), using the information gain ratio
743 as a splitting criterion. Model predictions were optimized with respect to maximal overall accuracy,
744 which reached 98.2%, meaning the underlying model is informative.

745 **Inter-feature relationship network mapping**

746 Data summarising phenotypic clusters 1, 4, 5 and 9 across each of the 15 key (feature-selected) Z-
747 normalized quantitative features was first selected. To ensure an equitable final comparison of inter-

748 feature relationship 'strengths' (i.e. uncertainty coefficient values), 1100 observations were randomly
749 sampled from each phenotypic cluster (as constrained by the smallest of these clusters (9), which
750 contains 1166 observations). The R package 'mpmi' was then used to calculate entropy values for each
751 quantitative feature and mutual information values between each pair of features. Mutual
752 information values for each feature pair were then independently normalized to the entropy value of
753 each feature pair-member, thus providing sensitivity to asymmetry in 'information overlap' as a
754 proportion of information captured within each feature. This constitutes an estimate of the
755 uncertainty coefficient in each 'direction' of inter-feature relationships. Uncertainty coefficient values
756 greater than 0.2 (thresholded to limit network connections and enable visual interpretation) were
757 plotted as directed edges in a circular 15 node (15 key features) network layout using the R package
758 'igraph'. Colour-coding and line thickness were defined by uncertainty coefficient values. Comparison
759 of networks using the igraph function 'difference' revealed how networks are re-wired in phenotypic
760 clusters 4, 5 and 9 when compared to cluster 1 (the main non-responsive, spontaneous phenotype
761 cluster).

762 **Time-series analysis of phenotypic trajectories**

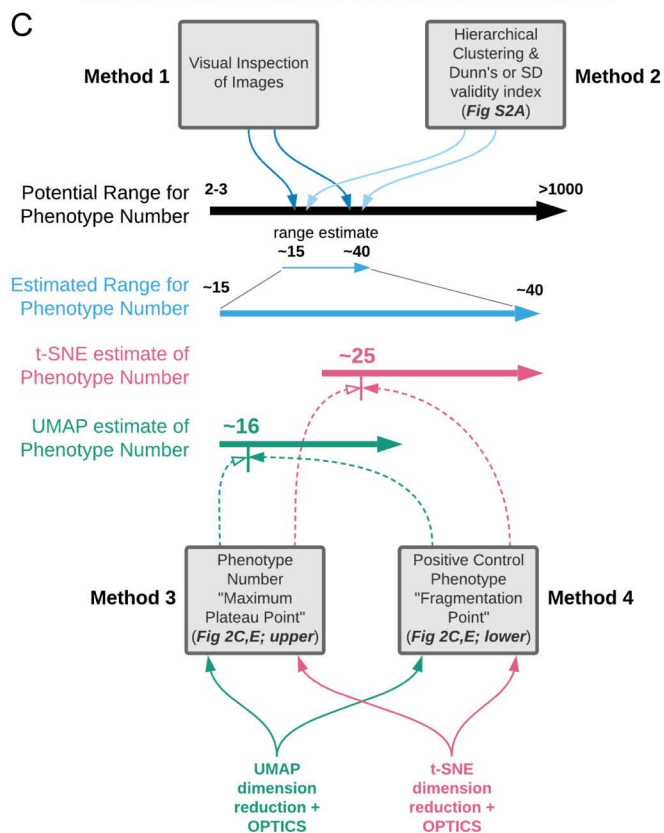
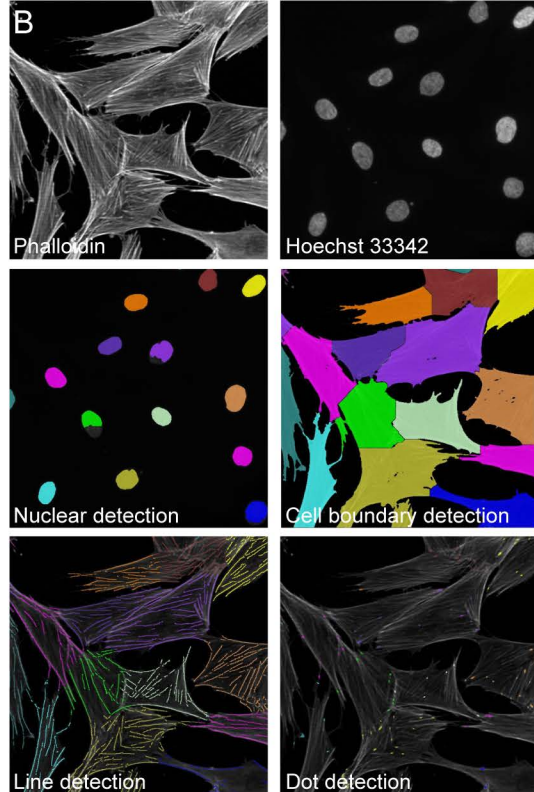
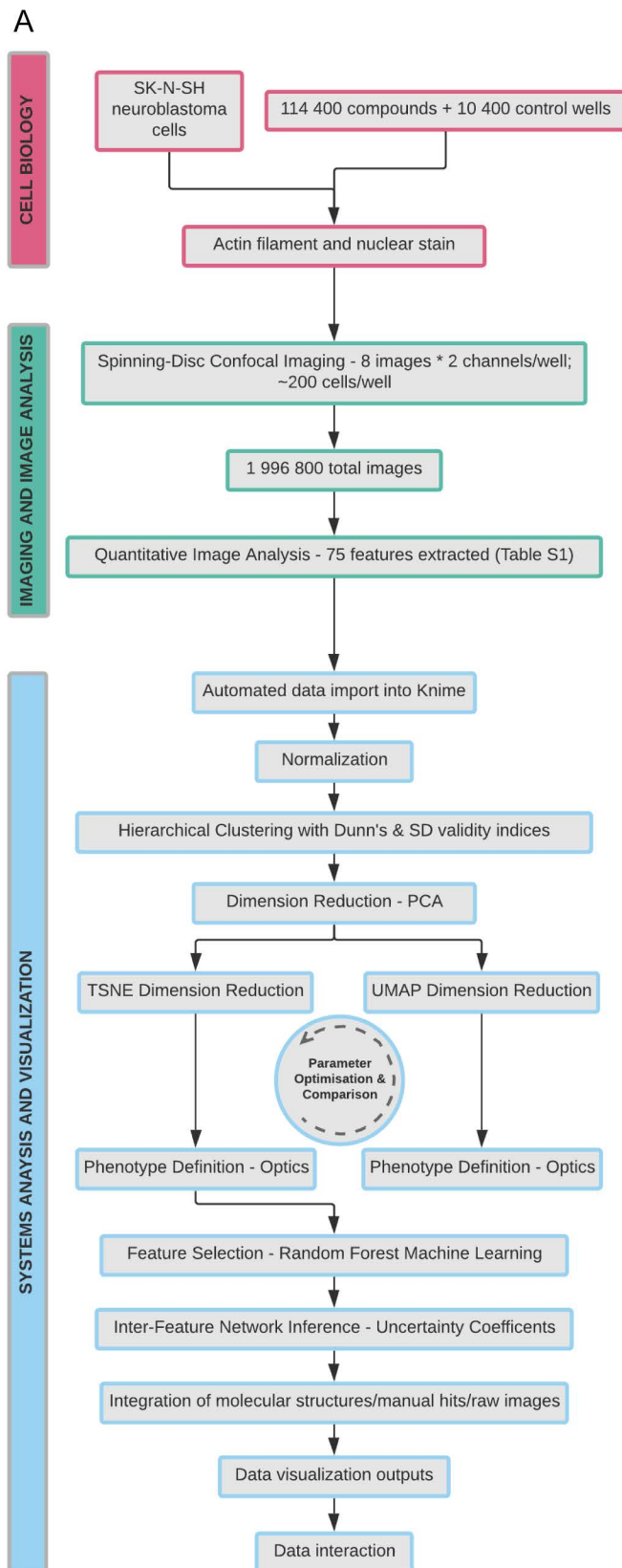
763 Data for time-series analysis of phenotypic trajectories was generated by parallel treatment of cells
764 with either negative control (DMSO), or 10 μ M of compounds T1 or T2. Cells were treated for periods
765 of 1 min, 5 min, 15 min, 30 min, 45 min, 1 h, 2 h, 3 h, 4 h, 6 h, 20 h or 24 h. Cells were fixed,
766 permeabilised and labelled, imaged and quantified as described for the main chemical perturbation
767 analyses. Statistical analyses mirrored the main chemical perturbation analyses, beginning with
768 exclusion of conditions capturing < 10 > 700 cells, Z-normalisation relative to DMSO controls, and
769 principle components analysis producing 26 orthogonal principle components as input for t-SNE
770 dimension reduction using a perplexity value of 50, as previously. Data were then filtered based on
771 comparison of loess regression (span = 1) in the presence and absence of putative outliers.
772 Independent dynamic phenotypic trajectories for compounds T1 and T2 were then estimated by fitting
773 a Bezier curve to all remaining values ordered by time. Data were plotted using R.

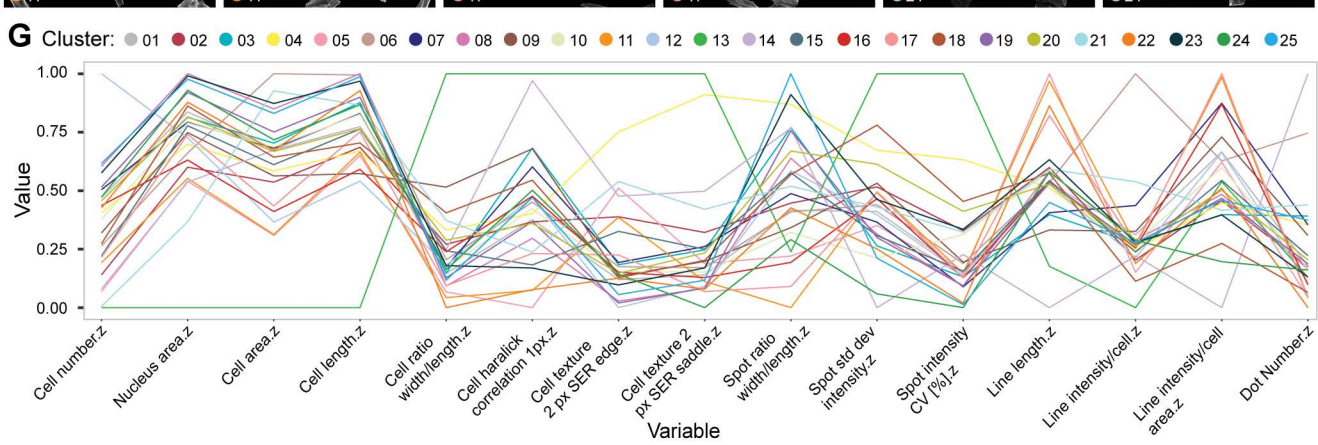
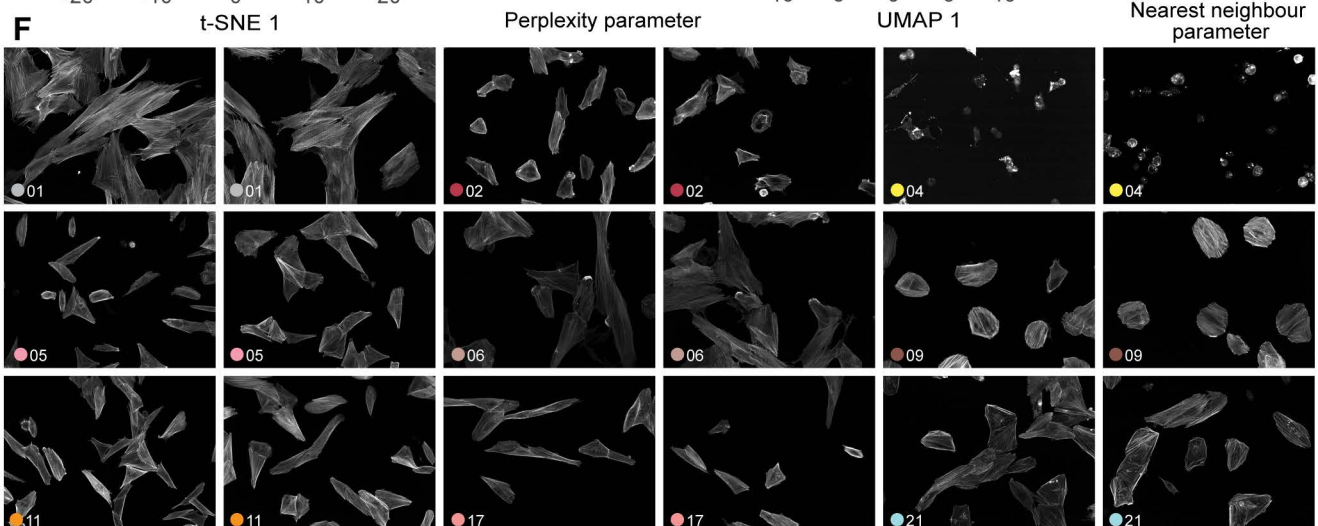
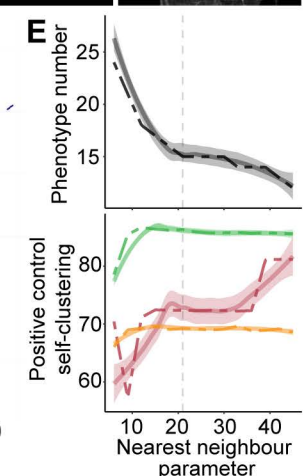
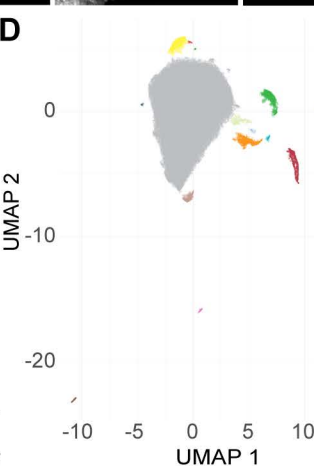
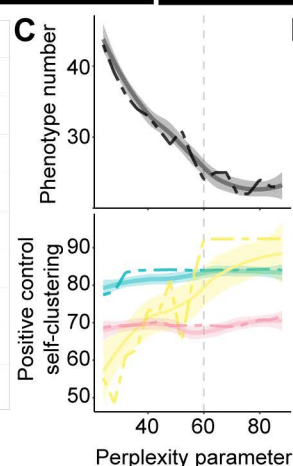
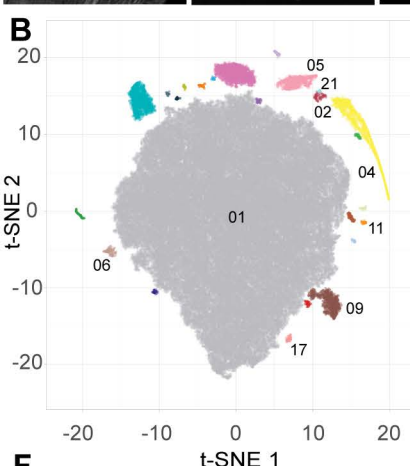
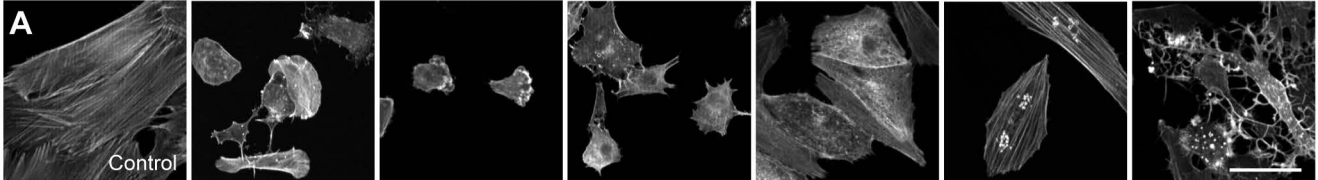
774 **Hierarchical clustering of phenotypes and features**

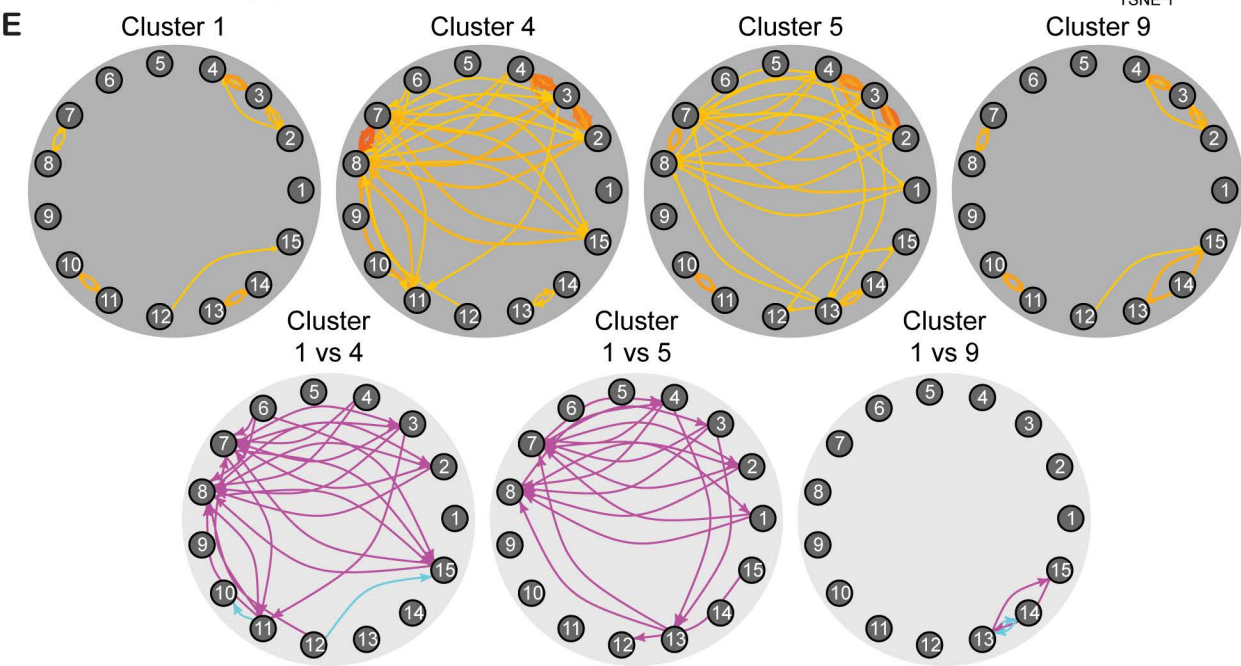
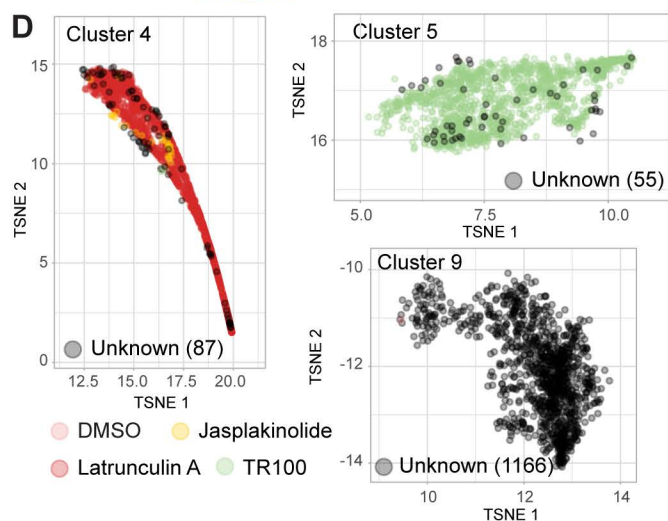
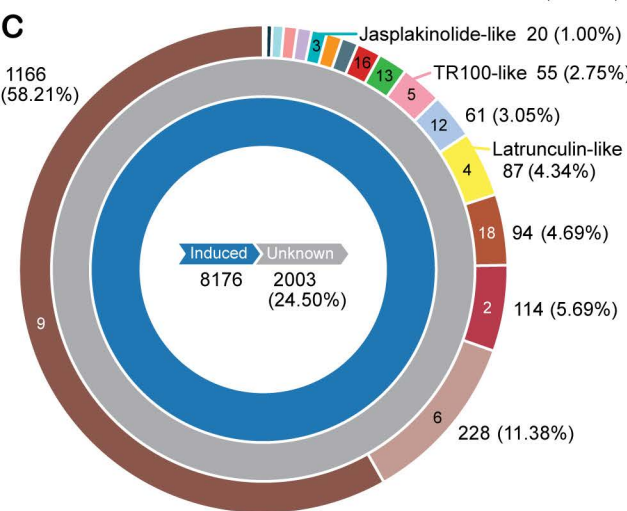
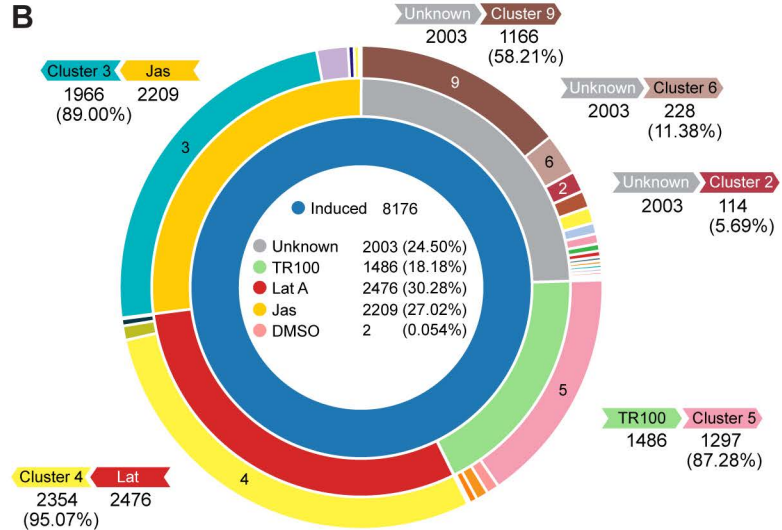
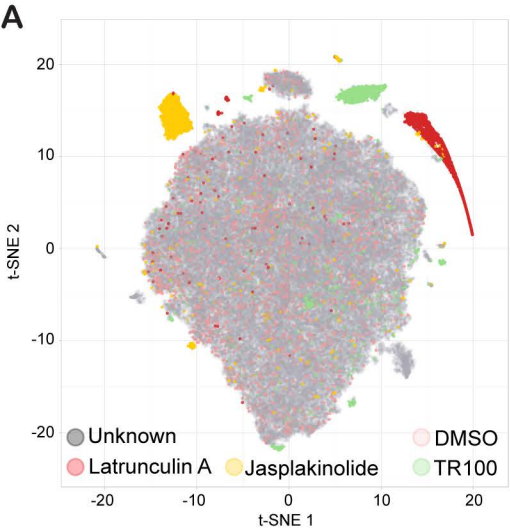
775 A heatmap summarising hierarchical clustering of all 25 phenotypic clusters and all 74 Z-normalized

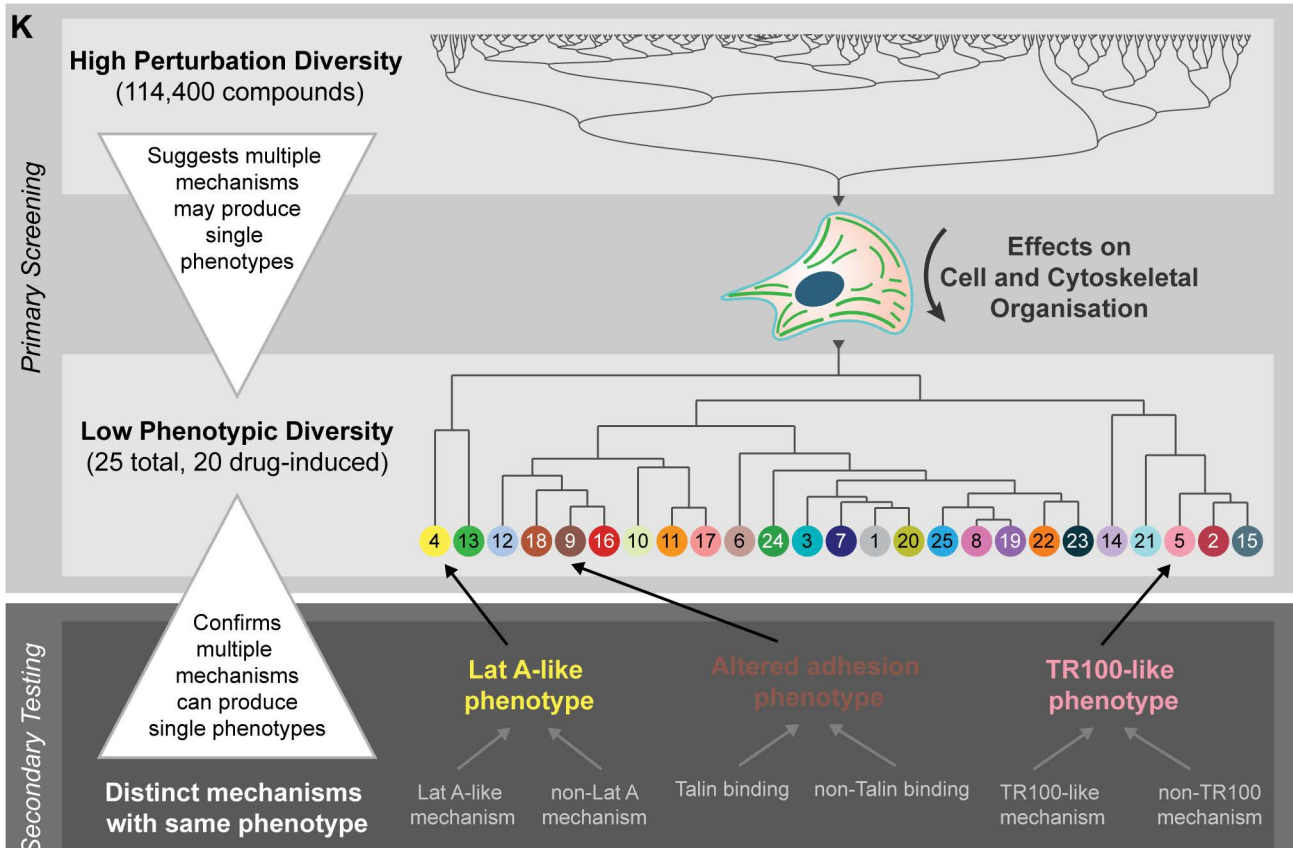
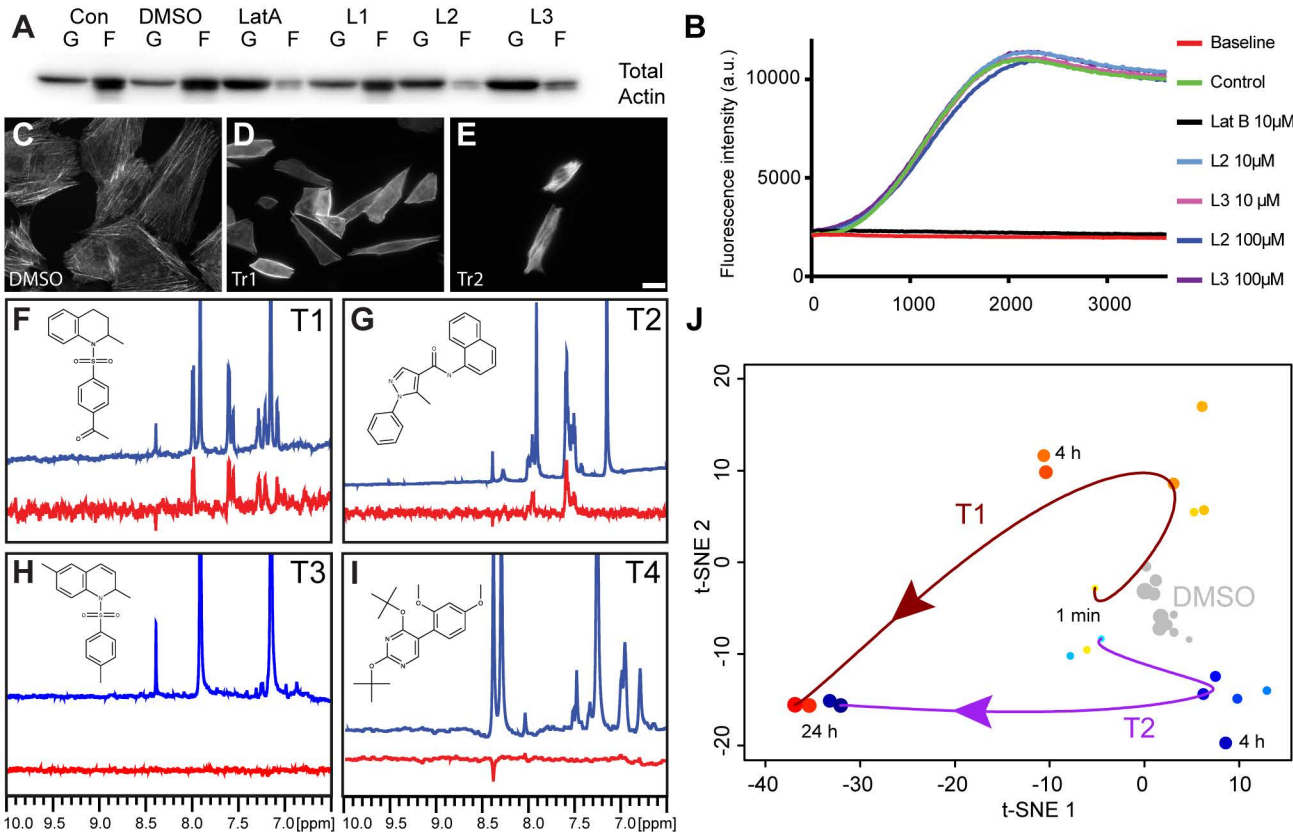
776 quantitative features was generated using the 'heatmap.2' function from the 'gplots' package in R.

777 Agglomerative clustering proceeded via complete linkage as described for the default 'hclust' function.









KEY RESOURCES TABLE

REAGENT or RESOURCE	SOURCE	IDENTIFIER
Antibodies		
C4 Total actin	Millipore	Cat# MAB1501, RRID:AB_2223041
γ9d Tpm3.1	Millipore	Cat# MAB2256, RRID:AB_10806918
Chemicals, Peptides, and Recombinant Proteins		
TR100	GVK Bio, India	Made to order
Latrunculin A	Adipogen Life Sciences	Cat# AG-CN2-0027-C500
Latrunculin B	Adipogen Life Sciences	Cat# AG-CN2-0031-M001
Jasplakinolide	Cayman Chemical	Cat#11705
Hoechst 33342	ThermoFisher Scientific	Cat#62249
Pyrene actin	Hypermol	Cat#8112-04
Critical Commercial Assays		
G-actin/F-actin <i>In Vivo</i> Assay Biochem Kit	Cytoskeleton	Cat# BK037
Experimental Models: Cell Lines		
Human Female: SK-N-SH neuroblastoma cells	ATCC	Cat# HTB-11, RRID:CVCL_0531
Recombinant DNA		
pmNeonGreen-talin	Shaner et al., 2013	
Software and Algorithms		
Columbus	Perkin Elmer	
Workspace	CSIRO	
Knime	https://www.knime.com/	
R	https://www.r-project.org/	
R-package ggplot2	https://ggplot2.tidyverse.org/	
R-package plotly	https://plot.ly/r/	
R-package NbClust	https://cran.r-project.org/web/packages/NbClust/index.html	
R-package Rtsne	https://cran.r-project.org/web/packages/Rtsne/index.html	
R-package dbscan	https://cran.r-project.org/web/packages/dbscan/index.html	
R-package mpmi	https://CRAN.R-project.org/package=mpmi	
R-package igraph	http://igraph.org/r/	

R-package gplots	https://cran.r-project.org/web/packages/gplots/index.html	
R-package Rtsne.multicore	https://github.com/DmitryUlyanov/Multicore-TSNE	
R-package UMAP	https://cran.r-project.org/web/packages/umap/index.html	
Lucidchart	https://www.lucidchart.com/	
Deposited Data		
DataDryad – Bryce_et_al_Quantitative_Data	doi:10.5061/dryad.1cg2dq2	